

Article

Investigation of the Microstructure and Mechanical Properties of an Ultrahigh Strength Martensitic Steel Fabricated Using Laser Metal Deposition Additive Manufacturing

Min Wang ^{1,2} , Qican Zhang ¹ , Wengang Li ³, Zhen Zhang ², Pengfei Chui ^{3,*}, Zhiting Yu ⁴ and Kun Zhang ^{5,6,*}

¹ College of Electronics and Information Engineering, Sichuan University, Chengdu 610065, China

² Automation Research Institute of China South Industries Group Corporation, Mianyang 621000, China

³ School of Materials Science and Engineering, Shaanxi University of Technology, Hanzhong 723001, China

⁴ DFH Satellite Co., Ltd., Beijing 100094, China

⁵ Key Laboratory of Microgravity (National Microgravity Laboratory), Institute of Mechanics, Chinese Academy of Sciences, Beijing 100190, China

⁶ School of Engineering Science, University of Chinese Academy of Sciences, Beijing 100049, China

* Correspondence: cuanpengfei@snut.edu.cn (P.C.); zhangkun@imech.ac.cn (K.Z.)

Abstract: Ultrahigh strength steels were additively manufactured (AM) using different batches of powders by means of the laser metal deposition (LMD) technique. After quenching and tempering treatments, the microstructures, mechanical properties, and fracture modes of ultrahigh strength steels were investigated by several testing methods. The results demonstrate that martensite and Fe₃C cementite were found in the three specimens after quenching and tempering treatments, and the tempered martensite microstructure had a lamellar structure in all specimens. The widths of these martensite lathes were observed to be different for the APHT-1, APHT-2, and APHT-3 samples, and their sizes were $1.92 \pm 0.90 \mu\text{m}$, $1.87 \pm 1.09 \mu\text{m}$, and $1.82 \pm 0.85 \mu\text{m}$, respectively. The martensitic steel exhibited excellent mechanical properties (tensile strength and impact toughness). The yield strength and the ultimate tensile strength of the APHT-3 sample reached 1582 MPa and 1779 MPa, respectively. Moreover, the value of the impact energy for the APHT-1 sample was 46.4 J. In addition, with the changes in the batches of ultrahigh strength steel powders, the fracture mode changed from ductile fracture to brittle fracture under tensile force and impact loads.

Keywords: additive manufacturing; ultrahigh strength steel; microstructure; mechanical properties; heat treatment



Citation: Wang, M.; Zhang, Q.; Li, W.; Zhang, Z.; Chui, P.; Yu, Z.; Zhang, K. Investigation of the Microstructure and Mechanical Properties of an Ultrahigh Strength Martensitic Steel Fabricated Using Laser Metal Deposition Additive Manufacturing. *Metals* **2022**, *12*, 1646. <https://doi.org/10.3390/met12101646>

Academic Editor: José Spinelli

Received: 11 August 2022

Accepted: 27 September 2022

Published: 30 September 2022

Publisher's Note: MDPI stays neutral with regard to jurisdictional claims in published maps and institutional affiliations.



Copyright: © 2022 by the authors. Licensee MDPI, Basel, Switzerland. This article is an open access article distributed under the terms and conditions of the Creative Commons Attribution (CC BY) license (<https://creativecommons.org/licenses/by/4.0/>).

1. Introduction

Additive manufacturing (AM) has attracted considerable attention in the field of machinery manufacturing due to its ability to make components layer by layer on the basis of a 3D-CAD volume model [1,2]. The advantages of this technology are that it is efficient, it avoids material waste, it reduces costs, and it overcomes the problems caused by traditional methods in manufacturing metal parts with complex shapes [3]. Therefore, additive manufacturing has been used in various fields, such as the aerospace, automotive, medical treatment, and energy industries [4,5]. Plenty of AM processes are widely used in 3D-printed metal materials, such as selective laser melting (SLM) [6], laser powder bed fusion (LPBF) [7], laser metal deposition (LMD) [8,9], wire and arc additive manufacturing (WAAM) [10], electron beam melting (EBM) [11], binder jetting (BJ) [12], and so on. LMD has attracted wide attention due to its high efficiency and dimensional accuracy. It utilizes a laser as the energy source. The metal powders are simultaneously delivered by a nozzle to the molten pool under computer-aided control [13], and the metal parts designed by the CAD model are obtained. A large number of metal parts made out of different metal alloys, including Ti-6Al-4V [14,15], Al-Si-Mg alloys [16], Cu alloys [17], nickel-based

superalloys [18,19], steels [20,21], and numerous other advanced alloys [22–24], have been successfully manufactured by laser metal deposition.

Ultrahigh strength steel is one kind of steel alloy used to manufacture structural parts bearing high stress and is widely applied in the aviation, aerospace, and military fields [25–28]. At present, there is interest in studying the mechanical properties of ultrahigh strength steels produced via selective laser melting. Raiyan [29] et al. utilized selective laser melting to prepare an AF9628 ultrahigh strength steel via optimizing process parameters, which was shown to exhibit strengths greater than 1.5 GPa with more than 10% tensile ductility due to the formation of an ϵ -carbide phase. Rahman Rashid [30] et al. reported the influence of a laser reheat post-treatment on the microstructural characteristics of laser-cladded ultrahigh strength steel. The hardness profile across the cladded regions of the as-deposited sample indicated the presence of hard (>650 HV) untempered martensite in both the clad and the heat-affected zone, whereas the hardness in the heat-affected zone decreased to about 500–590 HV after the laser post-heat treatment. Cameron et al. [31] studied the roles of deposition strategy and fill depth in the tensile properties of 300 M repaired through laser-directed energy deposition. The ultimate tensile strength was 1902 MPa for the 300M specimen repaired with the 10% effective repair depth via the track delay deposition strategy, whereas the ultimate tensile strength was reduced to 1560 MPa by the layer delay deposition strategy repaired with the 100% effective repair depth.

Impact toughness is the ability of a material to absorb plastic deformation work and fracture work under impact loading, reflecting the impact resistance of the material. It is a comprehensive performance test of material strength and plasticity, and it is an important mechanical property. Dilip et al. [32] reported that the impact energy of martensitic HY100 steel fabricated by SLM was approximately 24 J. After solution treatment, the impact energy increased a little, but it decreased sharply after solution treatment followed by ageing treatment. Raiyan [33] et al. manufactured ultrahigh strength martensitic steel AF9628 using laser powder bed fusion (LPBF). The Charpy impact toughness of the as-printed sample was approximately 28 J, but it was reduced to 24 J after quenching and tempering heat treatments. However, these results demonstrate that the impact toughness values of steels fabricated by the AM process are low, and further applications are limited. Hence, the key issue is to achieve high strength, plasticity, and impact toughness for AM steels.

The chemical compositions of different batches of gas-atomized steel powders are different in actual production, which may significantly affect the mechanical properties of the AM steels. However, there are few reports on the influence of different batches of steel powders on mechanical properties. In this work, our aim was to analyze the effects of different batches of ultrahigh strength steel powders on the microstructure and mechanical properties of the additively manufactured samples followed by heating treatment. A series of ultrahigh strength steels were manufactured using different batches of powders by laser metal deposition, and the microstructures and mechanical properties (tensile properties, hardness, and impact toughness) were investigated in depth.

2. Experimental Section

The experiments were performed using an LMD-1200 laser metal deposition machine (Automation Research Institute of China South Industries Group Corporation, Mianyang, China). A schematic diagram of the LMD machine is shown in Figure 1a. The forming quality of 3D-printed metal parts is influenced significantly by the process parameters [25]. The process parameters of LMD mainly include the laser powder, scanning speed, and overlap ratio. These parameters mainly depend on the chemical composition of the material. The laser power is too small to completely melt the powders. Conversely, if the power is too high, the molten pool may overheat, and the energy penetration may be too deep. The scanning speed is affected by the laser power and the size of the laser beam spot, and it cannot be too fast or too slow. If the overlap rate is not appropriate, it may lead to an insufficient curing area. In the previous study, orthogonal experiments were carried out, and the results were verified by a regression analysis.

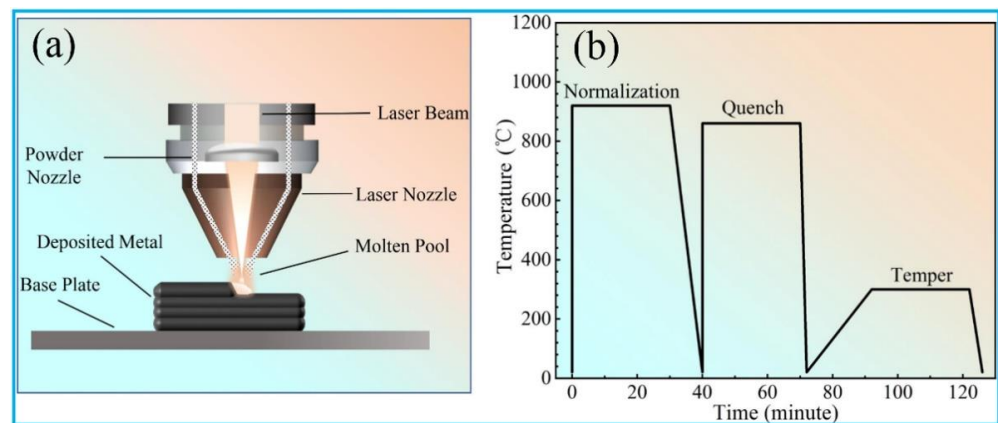


Figure 1. (a) Schematic diagram of the LMD machine. (b) Illustration of the heat treatment process.

The optimal experimental parameter was selected. The experimental process parameters were a laser power of 2000 W, a scanning speed of 10 mm/s, an overlap ratio of 50%, and a laser scan strategy with layers alternating by 90° in the x–y plane. Three samples with different batches of powders were printed using these parameters. The powder morphology of ultrahigh strength martensitic steel is approximately spherical, and its size is 50–150 μm , as shown in Figure 2. Before printing, the powder was dried in a vacuum oven (Shanghai Yiheng Technology Co., Ltd., Shanghai, China) for 2 h at 200 °C. The chemical compositions with different batches of powders are presented in Table 1. It has been clearly seen that the chemical compositions of powders change slightly in different batches, which may influence the microstructures and mechanical properties of as-printed samples. Low-carbon steel was selected as the base plate, which was annealed, polished, and cleaned, and then all samples were printed on this substrate.

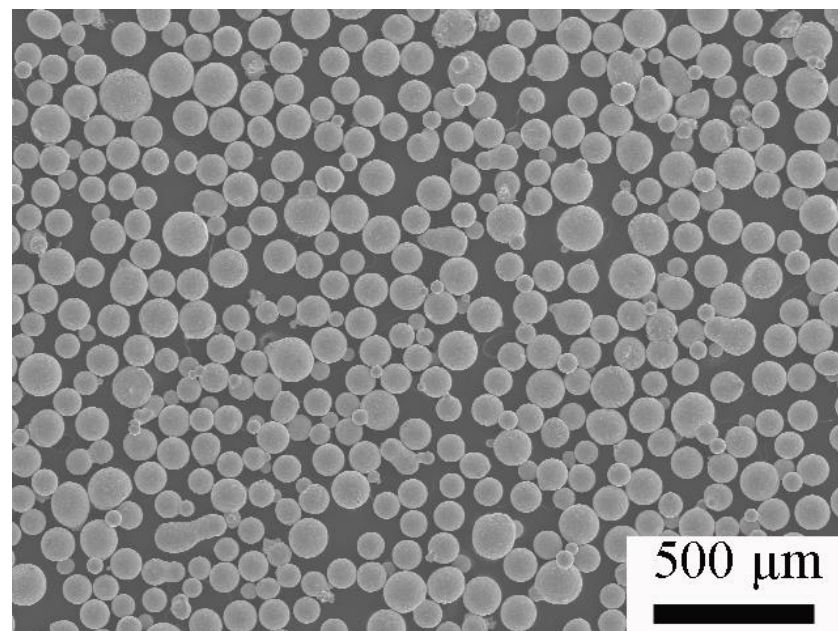


Figure 2. Powder morphology of ultrahigh strength martensitic steel.

Table 1. Chemical compositions of the ultrahigh strength steel in this study (wt. %).

Sample	Cr	Mn	Mo	Ni	Si	C	N	O
APHT-1	1.100	0.710	0.640	4.690	1.430	0.270	0.002	0.005
APHT-2	1.120	0.660	0.570	4.990	1.160	0.300	<0.003	0.009
APHT-3	1.140	0.650	0.580	5.240	1.890	0.320	0.003	0.002

To improve the ultrahigh strength martensitic steel, the as-printed specimens were heat-treated in a muffle furnace. The quenching and tempering processes were selected in our work according to the frequently used heat treatment process of the as-forged martensitic steel. In addition, due to the different cooling rates of each layer for the samples during printing, the variety of microstructures and mechanical properties were inconsistent in the as-printed materials. Therefore, a normalization treatment was necessary before quenching the as-printed specimens. All samples were treated according to the same heat treatment schedule. The detailed heat treatment process is described below and is illustrated in Figure 1b for visual clarity. The as-printed samples were treated by normalization at 920 °C for 30 min, air-cooled, austenitized at 860 °C for 30 min, oil cooled, tempered at 300 °C for 30 min, and then air-cooled to room temperature.

Some cubic specimens were cut from the three samples by wire electrical discharge machining to perform microstructural studies. The samples were polished to mirror-like surfaces with 400- to 1500-grade silicon carbide papers and then etched using a corrosion agent (a 5% nitric acid alcohol solution). A scanning electron microscopy (SEM) analysis was performed with a JSM-7610FPlus SEM equipped with EDS (JEOL Ltd., Tokyo, Japan). The determination of the phase compositions was carried out using an X-ray diffraction (XRD) instrument (Rigaku Corporation, Tokyo, Japan) with Cu- k_{α} radiation in a 2θ range of 20° to 100°.

All samples for testing the mechanical properties were cut perpendicular to the building direction by wire electrical discharge machining or a lathe operator. Rockwell hardness values were measured with an HRS-150 digital Rockwell hardness tester (Shanghai Zhongyan Instrument Manufacturing Factory, Shanghai, China). To ensure repeatability, each sample was analyzed five times, and the average values are reported. The room-temperature tensile tests were performed using an electromechanical universal testing machine (CMT5105, MTS Systems Co., Ltd, Shenzheng, China) equipped with an extensometer to obtain the axial strain. The dimensions of the dog-bone tensile specimens were 35 mm in length and 18 mm \times 3 mm \times 6 mm in the gage section. The strain rate for the three samples in each condition was $6.7 \times 10^{-4} \text{ s}^{-1}$ during loading until fracture. The Charpy impact measurements were carried out for three samples with a U-shaped notch using a ZBC2302-2 automatic impact testing machine (Shenzhen New Sansi Material Testing Co., Ltd., Shenzheng, China). The dimensions for the Charpy impact samples were 10 mm \times 10 mm \times 55 mm. To analyze the fracture mechanism, the micrographs of the fracture surfaces of the tensile samples and impact samples were characterized by SEM.

3. Results and Discussion

3.1. Microstructural Analysis

Optical micrographs of the three samples are shown in Figure 3a–c. Melt pool structures and heat-affected zones often appear in as-printed samples [32–34]. These interesting features have been reported in some studies [32,35] and may disappear after quenching and tempering. Therefore, the melt pool structures or heat-affected zones cannot be observed in Figure 3. In the three specimens, the microstructures were homogenous and were not obviously different from the optical images. In addition, cracks were not seen in any samples. This would suggest that the selected printing process and heat treatment schedule may be reasonable.

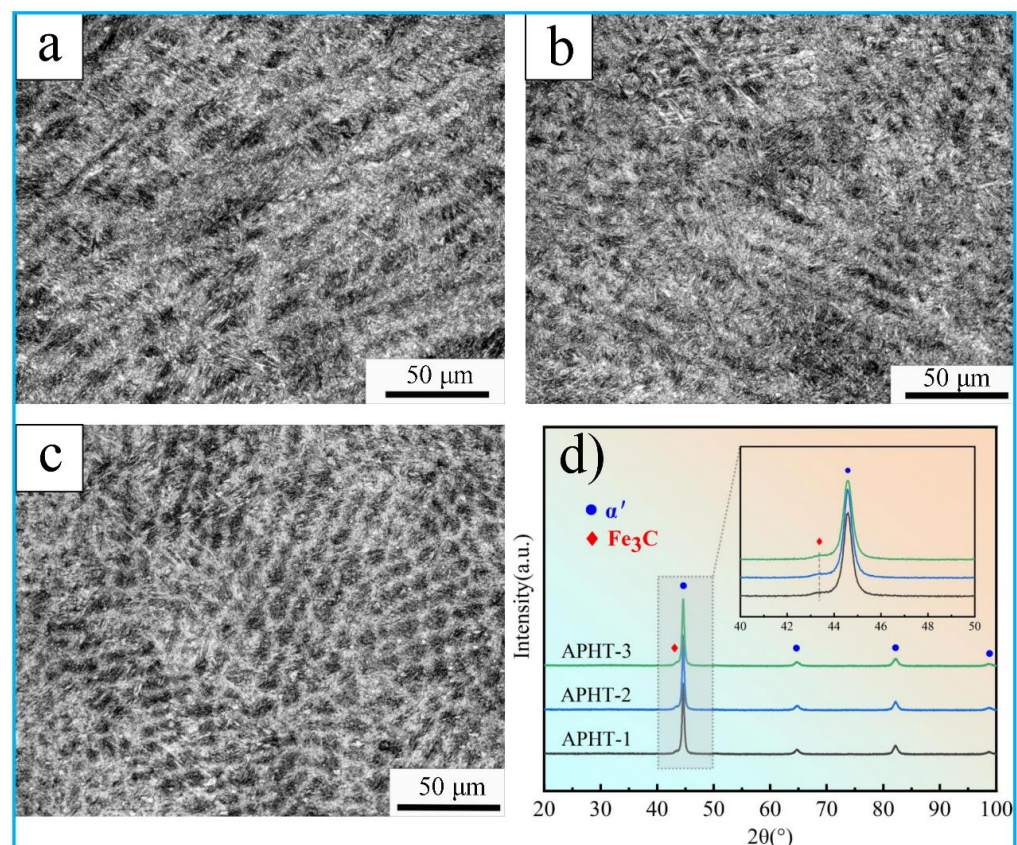


Figure 3. Optical micrographs and XRD patterns of three samples. (a) Optical micrograph of APHT-1. (b) Optical micrograph of APHT-2. (c) Optical micrograph of APHT-3. (d) XRD patterns of three samples.

Phase analyses of the three samples were carried out using X-ray diffraction. Figure 3d shows the XRD patterns of the samples. The diffraction peak positions were found at 44.6° , 64.6° , 82.1° , and 98.7° in each sample, and these peaks closely match the characteristic spectra of martensite. Additionally, a comparatively small peak at 43.2° was observed in each specimen, which closely matches the Fe_3C phase. It was noted that the diffraction peaks at 44.6° , 64.6° , 82.1° , and 98.7° also overlap with those of the Fe_3C phase. Similar results have been observed in an ultrahigh strength martensitic steel fabricated using selective laser melting [29]. In general, the formation of Fe_3C cementite in steel is mainly based on two aspects. On one hand, many ϵ -carbide particles precipitate from lath martensite during tempering. As the tempering temperature increases, the ϵ -carbide particles grow gradually and transform into Fe_3C . On the other hand, the retained austenite that appears after quenching could decompose into Fe_3C during tempering. Hence, the Fe_3C phase was found in the three samples. However, Fe_3C may provide favorable conditions for the formation and propagation of cracks, resulting in a decrease in the ductility of materials.

To further investigate the microstructures, higher-resolution micrographs of the three specimens were obtained using scanning electron microscopy (SEM), as shown in Figure 4a. A large number of tempered martensite microstructures with lamellar structures were observed in all specimens. A typical feature was martensite pockets with different sizes and orientations embedded in pre-existing austenite grains, and these martensite lathes were approximately parallel in arrangement. Although the diffraction peaks of the Fe_3C phase were found in the XRD patterns, it is difficult to see the Fe_3C precipitates in Figure 4. A possible reason is that the cementite precipitates formed during tempering were too fine to find by scanning electron microscopy. It is noteworthy that the sizes of these martensite lathes were observed to be different in the three samples. Comparing the APHT-2 and APHT-3 samples, the martensite lathes of the APHT-3 sample were rather

finer after heat treatment. This result reveals that the APHT-3 sample should possess excellent mechanical properties. Energy-dispersive spectrometry (EDS) maps of the APHT-1 sample are displayed in Figure 4b. Elemental segregation often occurs in many AM alloys during solidification due to low growth rates. However, a segregation of elements was not observed in the EDS maps for the APHT-1 sample. This indicates that the composition of the specimen was relatively homogeneous.

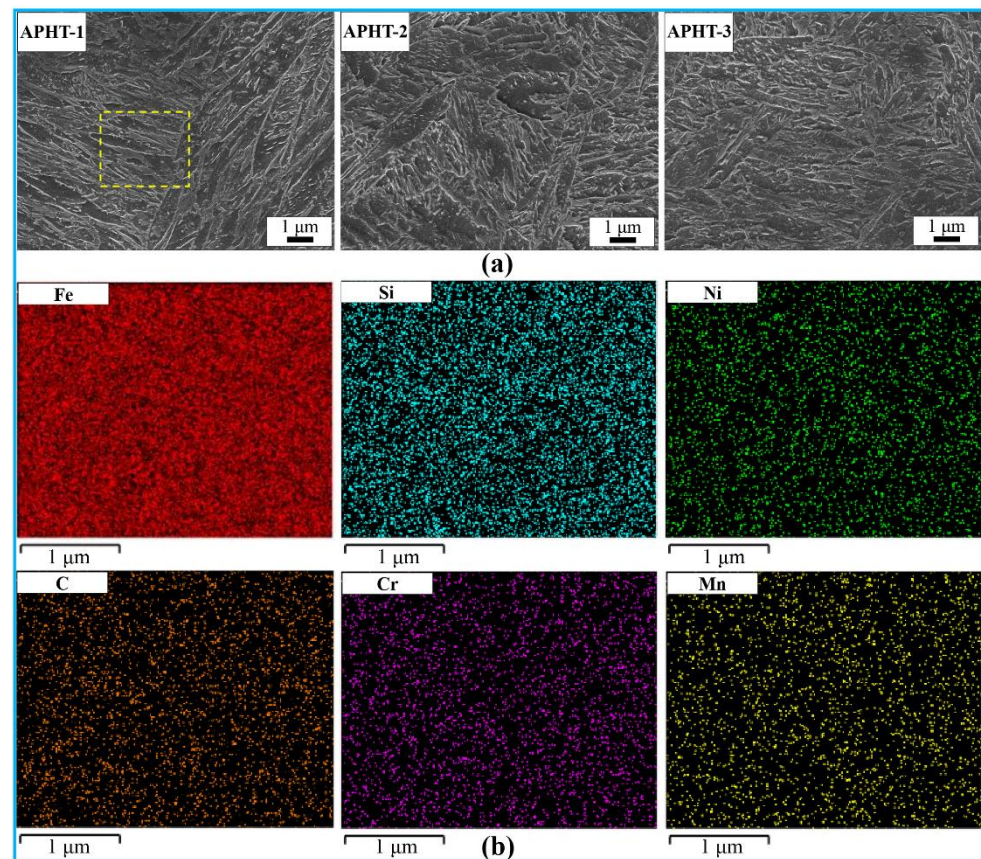


Figure 4. Microstructure images of three samples. (a) SEM micrograph of APHT-1, APHT-2 and APHT-3. (b) EDS maps of APHT-1. The yellow dotted lines in the APHT-1 provide a visual reference for EDS maps.

Electron backscattered diffraction (EBSD) images of the three samples are presented in Figure 5. Inverse pole figure (IPF) maps were used to analyze the microstructure of tempered martensite, as shown in Figure 5a. The martensite lath average equivalent diameters of each sample are displayed in Figure 5b, which were obtained by ImageJ© software [36]. The martensite lath sizes of APHT-1, APHT-2, and APHT-3 were $1.92 \pm 0.90 \mu\text{m}$, $1.87 \pm 1.09 \mu\text{m}$, and $1.82 \pm 0.85 \mu\text{m}$, respectively. There were slight changes in lath size, and the martensite lath size of APHT-3 was the smallest. This is consistent with the SEM results. The inverse pole figures shown in Figure 5c reveal the mesotexture of each specimen. The microstructures of the weak APHT-1 and APHT-3 martensite textures found in the [001] direction, aligned with the build direction, whereas APHT-2 had a weak bimodal texture along the [001] and [111] directions. Seede et al. [29] showed a similar weak $\langle 100 \rangle$ texture in their pole figures, aligned with the build direction, and this is consistent with our results.

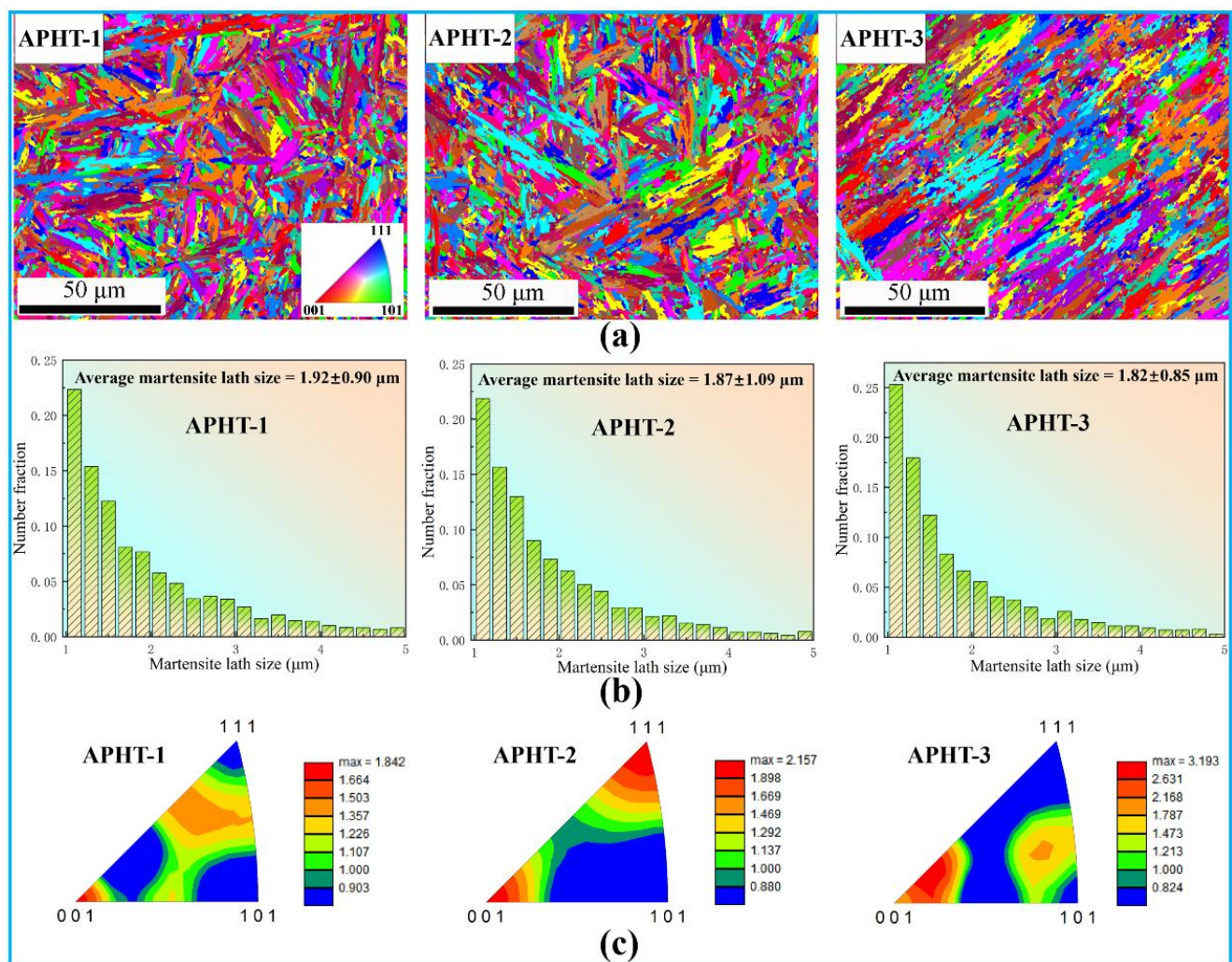


Figure 5. EBSD images of three samples: (a) inverse pole figure maps; (b) martensite lath size number fraction; (c) inverse pole figure.

3.2. Mechanical Properties

Due to the effect of building direction on the mechanical properties [37], all samples for testing the mechanical properties were cut perpendicular to the building direction. Figure 6 displays the mechanical properties of all specimens at room temperature. The mechanical property values (the yield strength, ultimate tensile strength, hardness, elongation, strain hardening exponent, and elastic energy) are presented in Table 2. The yield strength and ultimate tensile strength increased significantly with changing chemical compositions, up to 1582 MPa and 1779 MPa, respectively. This result exhibited a higher strength for the samples. However, the strain to fracture was found to be markedly reduced. In all samples, APHT-1 displayed excellent tensile mechanical properties due to its excellent strength and slightly high strain at fracture. In addition, the hardness of the three specimens increased slightly with the changing chemical compositions, which is consistent with the changed in strength. The hardness of APHT-3 was the highest, approximately 51.1 HRC.

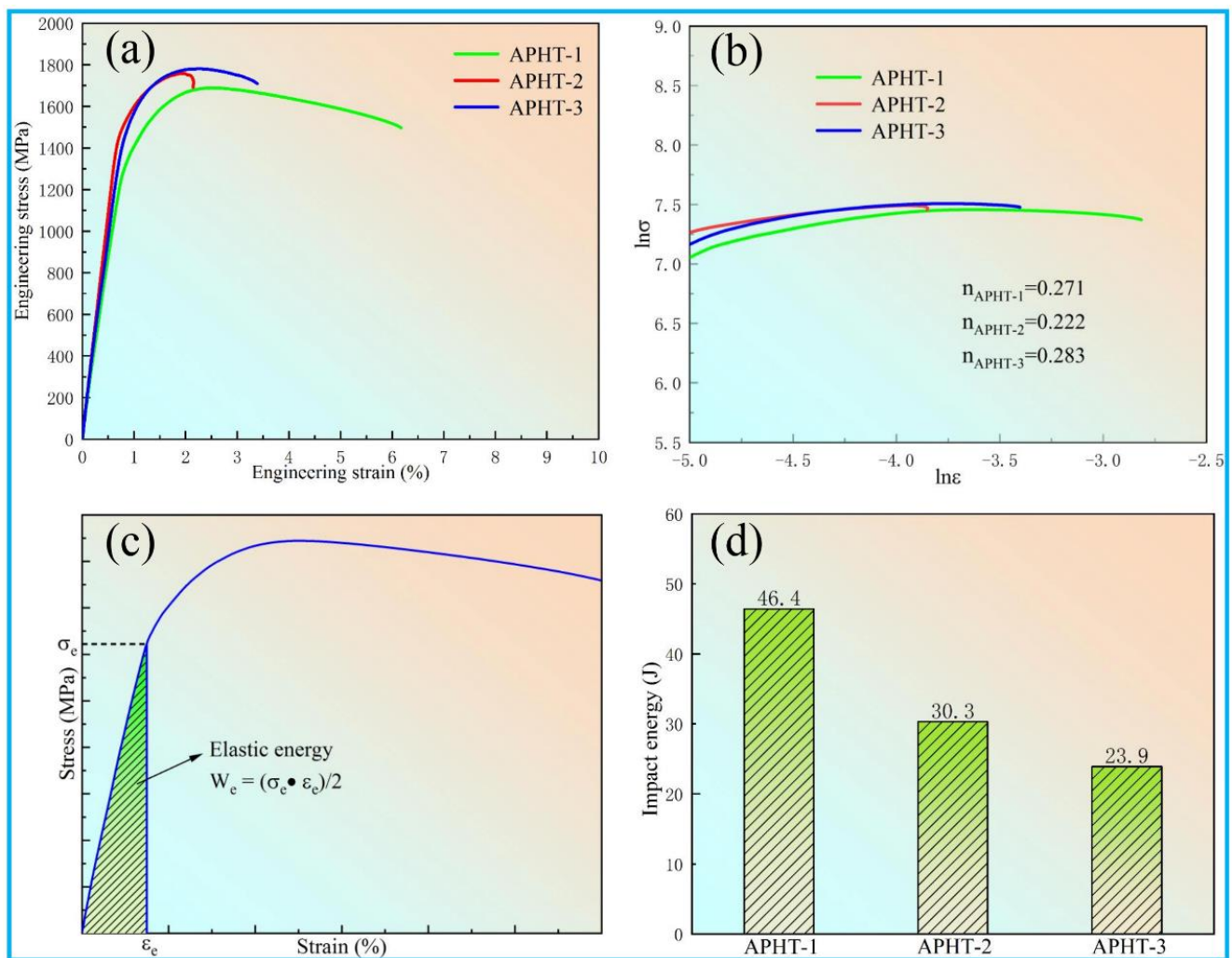


Figure 6. Mechanical property curves of all specimens at room temperature: (a) engineering stress–strain curves; (b) variation curves in $\ln\sigma$ with $\ln\epsilon$ for three samples; (c) diagram of elastic energy; (d) impact energy of samples.

Table 2. Mechanical property data of the ultrahigh strength steels.

Alloy	$\sigma_{0.2}$ (MPa)	σ_b (MPa)	Elongation (%)	Hardness (HRC)	n	W_e (MJ/m ³)
APHT-1	1413	1690	6.2	49.1	0.271	4.062
APHT-2	1568	1758	2.1	49.4	0.222	4.328
APHT-3	1582	1779	3.4	51.1	0.283	4.799

In the plastic deformation stage, shown in Figure 7a, the three specimens exhibited evident strain hardening, which can be explained by the following Hollomon [35,38] equation:

$$\sigma = K\epsilon^n \quad (1)$$

where σ is the true stress of the material, ϵ is the true strain, K is the hardening coefficient, and n is the strain hardening exponent. The strain hardening exponent (n) reflects the ability of the material to resist uniform plastic deformation [35,38]. When n is 1, the material is the ideal elastomer, and σ is directly proportional to ϵ ; when n is 0, $\sigma = K$, which indicates that the material is unable to undergo strain hardening [35,38].

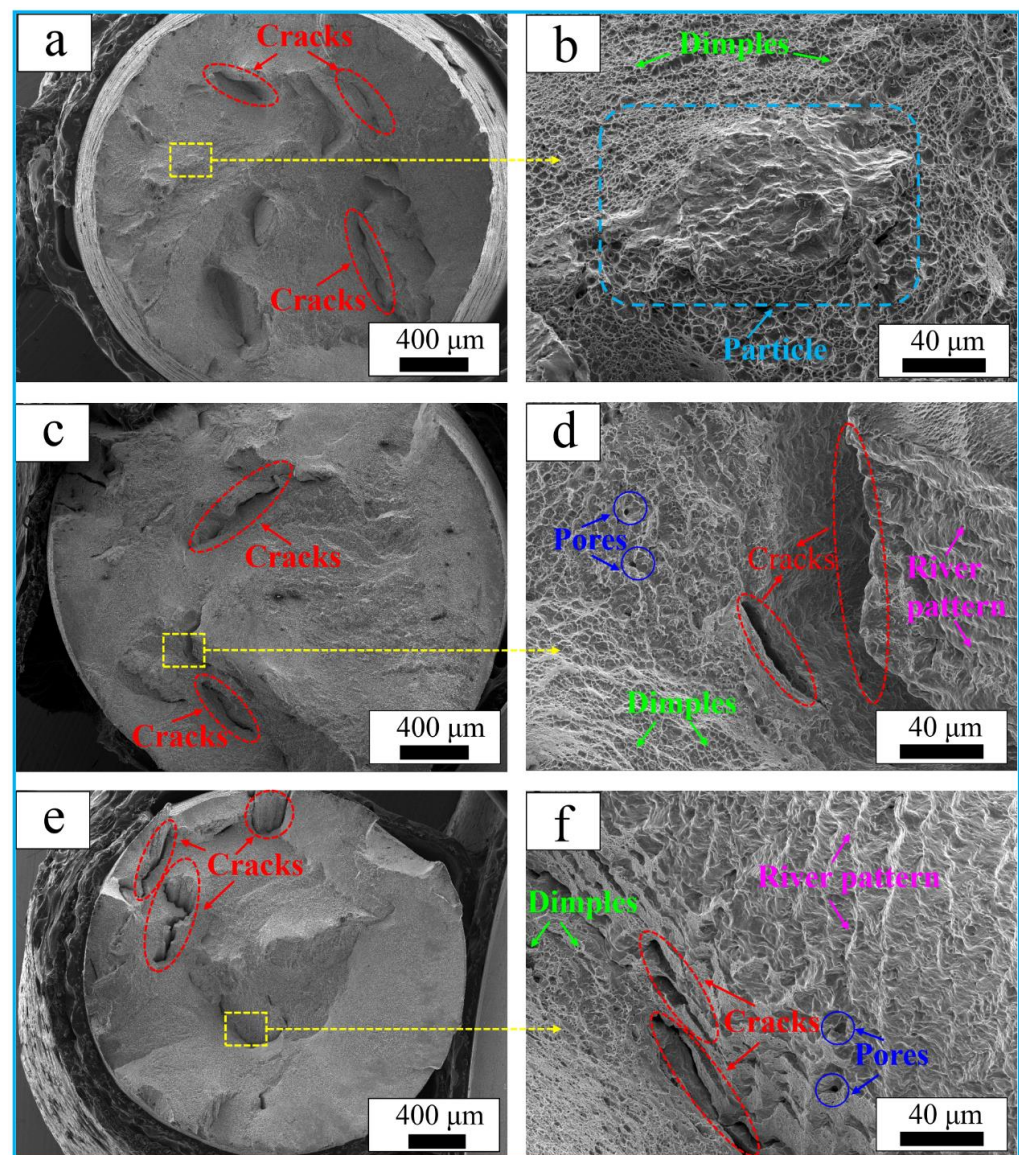


Figure 7. Micrographs of the fracture surfaces of the tensile-tested samples: (a,b) APHT-1; (c,d) APHT-2; (e,f) APHT-3.

To calculate the value of n , take the logarithm of both sides of Equation (1), and then the equation can be expressed as follows:

$$\ln \sigma = \ln K + n \ln \varepsilon \quad (2)$$

Figure 6b presents the variation curves in $\ln \sigma$ with $\ln \varepsilon$ for the three samples. The values of n are the slopes of the curves, which were calculated and are displayed in Table 2. The n values of all specimens ranged from 0.222 to 0.283. Compared with the other samples, APHT-3 had the highest value of n , which indicated a strong strain hardening ability. Although the n values were lower than that of copper, they were close to or higher than those of pure iron and common steels. Consequently, in the plastic deformation stage, the ultrahigh strength martensitic steels exhibited a strong strain hardening ability.

Elastic energy reflects the ability of a metal material to absorb elastic deformation work. It is an important index that is used to investigate the mechanical behavior of engineering materials. The diagram of elastic energy is shown in Figure 6c, and the shaded areas

represent the elastic energy. According to Equation (3), the elastic energy of a material can be calculated as:

$$W_e = \frac{1}{2} \sigma_e \varepsilon_e \quad (3)$$

where W_e is the elastic energy of the material, σ_e is the elastic limit, and ε_e is the elastic strain [39]. The elastic energy values of the ultrahigh strength martensitic steels were calculated using Equation (3), and they are displayed in Table 2. The elastic energy of the ultrahigh strength martensitic steels increased from 4.062 MJ/m³ to 4.799 MJ/m³ with the changing of the chemical compositions. The W_e value of APHT-1 was the highest among the three samples, and this can be attributed to the high elastic limit and elastic strain. Overall, the elastic energy values of the ultrahigh strength martensitic steels were substantially higher than that of spring steel (2.194 MJ/m³). Therefore, ultrahigh strength martensitic steels fabricated by LMD exhibited outstanding elastic deformation.

Figure 7 shows the micrographs of the fracture surfaces of the tensile-tested samples. Cracks can clearly be observed in the low-magnification SEM micrographs (Figure 7a,c,e) in all tensile-tested samples. Compared with the APHT-1 sample, the cracks of the APHT-2 and APHT-3 samples were wider and deeper, which indicates early failure and fracture during stretching. It is noteworthy that a large number of dimples can be seen in Figure 7b, which indicates that the APHT-1 sample mostly had ductile fractures. At the same time, a large particle of approximately 100 µm can also be seen in Figure 7b. Under an external force, dislocation pile-ups occur at the interface between particles and the matrix, and this stimulates the nucleation of microcracks. Therefore, it is detrimental to the ductility of materials. Therefore, although many dimples appeared in the fractured surface of the APHT-1 sample, the strain to failure was only 6.2%. In Figure 7d,f, torn edges, cracks, and a small number of dimples can be seen in the fracture surface. The results reveal that the failure modes were composed of ductile fracture and brittle fracture in the APHT-2 and APHT-3 samples. However, brittle fractures were dominant during the tensile testing. Hence, the strain to failure values of the APHT-2 and APHT-3 samples were lower than that of the APHT-1 samples.

The toughness of a material is a measure of its ability to absorb energy during its plastic deformation and sudden fracture and indicates the impact resistance of the material. Impact toughness is the synthesis of the strength and ductility. The results of the Charpy impact tests of the three samples are shown in Table 2. The impact energies of APHT-1, APHT-2, and APHT-3 were 46.4 J, 30.3 J, and 23.9 J, respectively. APHT-1 displayed the maximum impact energy when compared with APHT-2 and APHT-3, revealing great impact toughness.

Figure 8 shows the micrographs of the fracture surfaces obtained from the Charpy impact samples. Figure 8b,d,f are high-magnification images, which demonstrate the fracture modes of the Charpy impact specimens. A large number of deformed dimples of different sizes were observed in the fracture surface of the APHT-1 sample, revealing that the sample possessed great toughness. However, only a small quantity of dimples, lath packets, and some cracks are clearly seen in Figure 8d,f, showing that the APHT-2 and APHT-3 samples were very brittle. In addition, low-magnification optical images of the fracture surface are presented in Figure 8g. Shear lips were found on the fracture surfaces of all impact specimens. The higher the ductility of the material and the lower the crack growth rate, the higher the proportion of shear lip in the fracture width. The shear lip width of the APHT-1 sample was wider than those of the APHT-2 and APHT-3 samples. Hence, the toughness of the APHT-1 sample was the greatest.

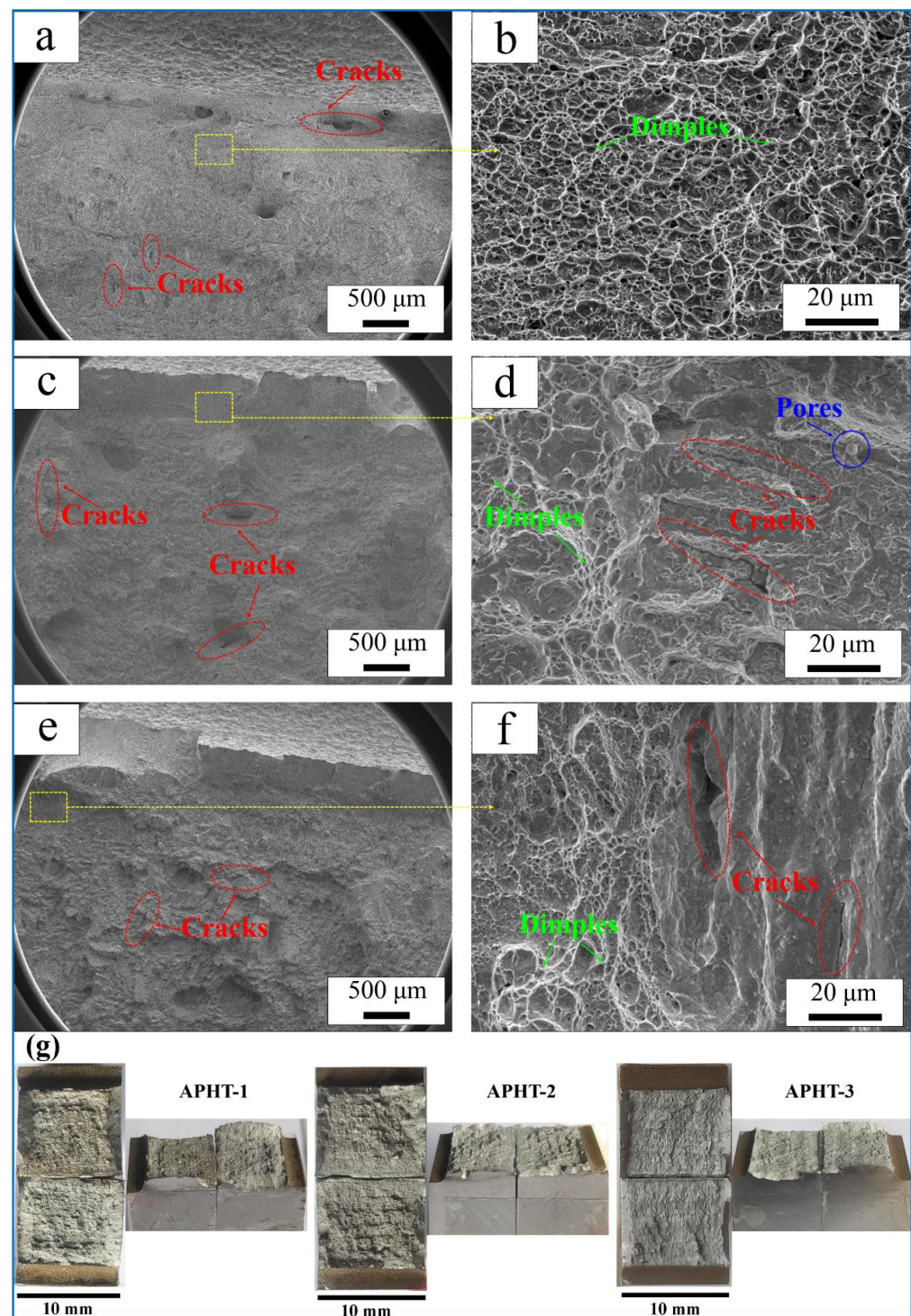


Figure 8. Micrographs of the fracture surfaces for the Charpy impact samples: (a,b) APHT-1; (c,d) APHT-2; (e,f) APHT-3; (g) low-magnification optical images of three samples.

4. Discussion

According to the SEM and EBSD results, the microstructures of ultrahigh strength steels slightly changed with the chemical composition. The martensite lath sizes of APHT-1, APHT-2, and APHT-3 decreased gradually. It is widely known that the lath width of martensite is related to the pre-existing austenite grain size due to structural inheritance. The smaller the pre-existing austenite grain size during austenitization, the smaller the lath martensite after quenching. The pre-existing austenite grain size depends on the quenching temperature. Consequently, the quenching temperature has a significant influence on the

martensite lath size and mechanical properties [40]. In general, the quenching temperature of hypoeutectoid steel is proposed to be $Ac_3 + (30\text{--}50)^\circ\text{C}$. Ac_3 is connected with the content of carbon and alloy elements, which can be obtained by the following empirical equation (all elements in wt.%).

$$Ac_3 = 910 - 203 \times C^{1/2} \times 15.2 \text{ Ni} + 44.7 \text{ Si} + 104 \text{ V} + 31.5 \text{ Mo} + 13.1 \text{ W} \quad (4)$$

Based on the data presented in Table 1 and Equation (4), the Ac_3 values of APHT-1, APHT-2, and APHT-3 were approximately 793°C , 817°C , and 818°C , respectively. Accordingly, the quenching temperature (860°C) that was selected for the ultrahigh strength steels was reasonable (discussed in Section 2). In addition, although the three samples were treated under the same quenching temperature at 860°C , the quenching temperature of APHT-1 was higher than those of APHT-2 and APHT-3 due to the low Ac_3 value. Therefore, APHT-1 had the largest martensite lath size, and APHT-3 had the smallest martensite lath size. This is consistent with the EBSD results.

The mechanical property results showed that the strength of ultrahigh strength steels increased in an orderly manner with the change in composition, and the yield strength and ultimate tensile strength values of APHT-3 were the highest. Lath martensite was formed in the ultrahigh strength steels after quenching, and the supersaturation of martensite decreased after tempering. According to the SEM and EBSD results, the lath martensite sizes were slightly different. This situation may lead to changes in the strength. Based on the Hall–Petch relationship, since the lath martensite size of APHT-3 was the smallest, its strength was the highest.

Additionally, the impact toughness for industrial steel is also an important mechanical property index. It is very difficult to combine both strength and toughness in ultrahigh strength steels prepared by means of additive manufacturing. In this work, the impact toughness of APHT-1 was the highest, approximately 46.4 J. This was because APHT-1 had excellent strength and ductility after the quenching and tempering treatments. Bai et al. [41] reported that a maraging steel fabricated by selective laser melting exhibited a lower impact toughness ($<20 \text{ J}$) after a heating treatment than APHT-1 when their strengths are similar. Liu et al. [42] explored the impact toughness of 300 M ultrahigh strength steel prepared by additive manufacturing. That study showed that the impact toughness was less than 30 J. Hence, the APHT-1 prepared in our work had excellent impact toughness.

5. Conclusions

In this study, ultrahigh strength steels were fabricated using different batches of powders via laser metal deposition. After heat treatment, the microstructures and mechanical properties of the steels were investigated. The following conclusions were drawn:

- The diffraction peaks of martensite and Fe_3C cementite were found in the three specimens after the quenching and tempering treatments. The appearance of Fe_3C cementite comes from the transformation of ϵ -carbide particles and retained austenite during tempering.
- A large number of tempered martensite microstructures with lamellar structures were observed in all specimens. Due to the changes in the chemical compositions, the widths of these martensite lathes were observed to be different in the three samples, and their sizes in APHT-1, APHT-2, and APHT-3 were $1.92 \pm 0.90 \mu\text{m}$, $1.87 \pm 1.09 \mu\text{m}$, and $1.82 \pm 0.85 \mu\text{m}$, respectively. The martensite lath size of APHT-3 was the smallest.
- Ultrahigh strength steels manufactured by LMD exhibit outstanding mechanical properties. The three specimens displayed the yield strengths varying from 1413 MPa to 1582 MPa, and their ultimate tensile strength increased from 1690 MPa to 1779 MPa. The strength of APHT-3 was the highest among all specimens. The impact energy values of the three samples were in the range of 23.9 J to 46.4 J, and the impact toughness of APHT-1 was the highest after the quenching and tempering treatments.

A large number of deformed dimples with different sizes were observed in the fracture surface of APHT-1. With the changes in the batches of ultrahigh strength steel powders, the fracture modes changed from ductile fracture to brittle fracture under tensile force and impact loads.

Author Contributions: Conceptualization, Q.Z.; Investigation, M.W.; Data curation, W.L., Z.Z. and Z.Y.; Writing—original draft, P.C.; Writing—review & editing, Z.Y. and K.Z. All authors have read and agreed to the published version of the manuscript.

Funding: The authors gratefully acknowledge the financial support from the Sichuan Province Science and Technology Major Project (Grant No. 2020ZDZX0014) and the National Natural Science Foundation of China (Grant No. 12272392).

Institutional Review Board Statement: Not applicable.

Informed Consent Statement: Not applicable.

Data Availability Statement: Not applicable.

Conflicts of Interest: The authors declare no conflict of interest.

Nomenclature

$\sigma_{0.2}$	yield strength
σ	true stress of the material
K	hardening coefficient
W_e	elastic energy of the material
σ_b	ultimate tensile strength
ϵ	true strain
n	strain hardening exponent
σ_e	elastic limit
ϵ_e	elastic strain

References

- Shahwaz: Nath, P.; Sen, I. A critical review on the microstructure and mechanical properties correlation of additively manufactured nickel-based superalloys. *J. Alloy. Compd.* **2022**, *907*, 164530. [\[CrossRef\]](#)
- Korkmaz, M.E.; Gupta, M.K.; Robak, G.; Moj, K.; Krolczyk, G.M.; Kuntoğlu, M. Development of lattice structure with selective laser melting process: A state of the art on properties, future trends and challenges. *J. Manuf. Process.* **2022**, *81*, 1040–1063. [\[CrossRef\]](#)
- Korkmaz, M.E.; Gupta, M.K.; Waqar, S.; Kuntoğlu, M.; Krolczyk, G.M.; Maruda, R.W.; Pimenov, D.Y. A short review on thermal treatments of titanium & nickel based alloys processed by selective laser melting. *J. Mater. Res. Technol.* **2021**, *16*, 1090–1101. [\[CrossRef\]](#)
- Li, N.; Huang, S.; Zhang, G.; Qin, R.; Liu, W.; Xiong, H.; Shi, G.; Blackburn, J. Progress in additive manufacturing on new materials: A review. *J. Mater. Sci. Technol.* **2019**, *35*, 242–269. [\[CrossRef\]](#)
- Culmone, C.; Smit, G.; Breedveld, P. Additive manufacturing of medical instruments: A state-of-the-art review. *Addit. Manuf.* **2019**, *27*, 461–473. [\[CrossRef\]](#)
- Ji, H.; Gupta, M.K.; Song, Q.; Cai, W.; Zheng, T.; Zhao, Y.; Liu, Z.; Pimenov, D.Y. Microstructure and machinability evaluation in micro milling of selective laser melted Inconel 718 alloy. *J. Mater. Res. Technol.* **2021**, *14*, 348–362. [\[CrossRef\]](#)
- Shakerin, S.; Hadadzadeh, A.; Amirkhiz, B.S.; Shamsdini, S.; Li, J.; Mohammadi, M. Additive manufacturing of maraging steel-H13 bimetal using laser powder bed fusion technique. *Addit. Manuf.* **2019**, *29*, 100797. [\[CrossRef\]](#)
- Karimbaev, R.M.; Cho, I.S.; Pyun, Y.S.; Amanov, A. Effect of ultrasonic nanocrystal surface modification treatment at room and high temperatures on the high-frequency fatigue behavior of Inconel 718 fabricated by laser metal deposition. *Metals* **2022**, *12*, 515. [\[CrossRef\]](#)
- Xu, W.; Bai, X.; Sun, Z.; Meng, X.; Guo, Z. Correlation between laser-ultrasound and microstructural properties of laser melting deposited Ti6Al4V/B₄C composites. *Metals* **2021**, *11*, 1951. [\[CrossRef\]](#)
- Chaudhari, R.; Parmar, H.; Vora, J.; Patel, V.K. Parametric study and investigations of bead geometries of GMAW-based wire-arc additive manufacturing of 316L stainless steels. *Metals* **2022**, *12*, 1232. [\[CrossRef\]](#)
- Wang, S.; Tao, S.; Peng, H. Influence of powder characteristics on the microstructure and mechanical behaviour of GH4099 superalloy fabricated by electron beam melting. *Metals* **2022**, *12*, 1301. [\[CrossRef\]](#)

12. Tang, Y.; Huang, Z.; Yang, J.; Xie, Y. Enhancing the capillary force of binder-jetting printing Ti6Al4V and mechanical properties under high temperature sintering by mixing fine powder. *Metals* **2020**, *10*, 1354. [\[CrossRef\]](#)
13. Kang, X.; Dong, S.; Men, P.; Liu, X.; Yan, S.; Wang, H.; Xu, B. Microstructure evolution and gradient performance of 24CrNiMo steel prepared via laser melting deposition. *Mater. Sci. Eng. A* **2020**, *777*, 139004. [\[CrossRef\]](#)
14. Liu, Q.; Wang, Y.; Zheng, H.; Tang, K.; Ding, L.; Li, H.; Gong, S. Microstructure and mechanical properties of LMD–SLM hybrid forming Ti6Al4V alloy. *Mater. Sci. Eng. A* **2016**, *660*, 24–33. [\[CrossRef\]](#)
15. Raju, R.; Duraiselvam, M.; Petley, V.; Verma, S.; Rajendran, R. Microstructural and mechanical characterization of Ti6Al4V refurbished parts obtained by laser metal deposition. *Mater. Sci. Eng. A* **2015**, *643*, 64–71. [\[CrossRef\]](#)
16. Jandaghi, M.R.; Pouraliakbar, H.; Fallah, V.; Ghassemali, E.; Saboori, A.; Pavese, M. Additive manufacturing of nano-oxide decorated AlSi₁₀Mg composites: A comparative study on Gd₂O₃ and Er₂O₃ additions. *Mater. Charact.* **2022**, *192*, 112206. [\[CrossRef\]](#)
17. Liu, Y.; Ye, Z.; Wang, X.; Liang, B.; Zhang, Y. Microstructure and mechanical behavior of Cu–9Al–4Ni–3.5Fe–0.5Mn alloy fabricated by laser melting deposition. *Mater. Sci. Eng. A* **2021**, *826*, 142006. [\[CrossRef\]](#)
18. Li, W.; Di, R.; Yuan, R.; Song, H.; Lei, J. Microstructure, wear resistance and electrochemical properties of spherical/non-spherical WC reinforced Inconel 625 superalloy by laser melting deposition. *J. Manuf. Process.* **2022**, *74*, 413–422. [\[CrossRef\]](#)
19. Zhang, J.; Huang, Z.; Fang, Y.; Gu, Z.; Xie, J.; Lei, J. Experiments and numerical simulations for the mechanical properties of Ni-based superalloys fabricated by laser melting deposition. *Opt. Laser Technol.* **2021**, *140*, 107058. [\[CrossRef\]](#)
20. Feng, J.; Zhang, P.; Jia, Z.; Yu, Z.; Fang, C.; Yan, H.; Shi, H.; Tian, Y. Microstructures and mechanical properties of reduced activation ferritic/martensitic steel fabricated by laser melting deposition. *Fusion Eng. Des.* **2021**, *173*, 112865. [\[CrossRef\]](#)
21. He, Y.; Wei, J.; Liu, J.; Wang, X.; Wang, Y.; He, L. Experimental study on the fabrication profile and mechanical properties by substrate-inclined angle using laser melting deposition (LMD) integrating with the substrate of stainless steel. *Opt. Laser Technol.* **2019**, *125*, 106038. [\[CrossRef\]](#)
22. Pang, Z.; Yang, J.; Manladan, S.M.; Cai, Y.; Han, J. Effect of high-temperature heat treatment on strengthening mechanism of AlCoCrFeNi component fabricated by LMD. *Metals* **2022**, *12*, 767. [\[CrossRef\]](#)
23. Cai, Y.; Shan, M.; Cui, Y.; Manladan, S.M.; Lv, X.; Zhu, L.; Sun, D.; Wang, T.; Han, J. Microstructure and properties of FeCoCrNi high entropy alloy produced by laser melting deposition. *J. Alloy. Compd.* **2021**, *887*, 161323. [\[CrossRef\]](#)
24. Peng, H.; Xie, S.; Niu, P.; Zhang, Z.; Yuan, T.; Ren, Z.; Wang, X.; Zhao, Y.; Li, R. Additive manufacturing of Al_{0.3}CoCrFeNi high-entropy alloy by powder feeding laser melting deposition. *J. Alloy. Compd.* **2021**, *862*, 158286. [\[CrossRef\]](#)
25. Bai, Y.; Yang, Y.; Wang, D.; Zhang, M. Influence mechanism of parameters process and mechanical properties evolution mechanism of maraging steel 300 by selective laser melting. *Mater. Sci. Eng. A* **2017**, *703*, 116–123. [\[CrossRef\]](#)
26. Sun, J.; Nitschke-Pagel, T.; Dilger, K. Influence of temperature- and phase-dependent yield strength on residual stresses in ultra-high strength steel S960 weldments. *J. Mater. Res. Technol.* **2021**, *15*, 1854–1872. [\[CrossRef\]](#)
27. Guo, X.; Liu, S.; Xu, J.; Wang, S.; Fu, L.; Chai, Z.; Lu, H. Effect of step cooling process on microstructures and mechanical properties in thermal simulated CGHAZ of an ultra-high strength steel. *Mater. Sci. Eng. A* **2021**, *824*, 141827. [\[CrossRef\]](#)
28. Mandal, A.; Ghosh, A.; Chakrabarti, D.; Davis, C. Effect of coiling temperature on impact toughness of hot rolled ultra-high-strength multiphase steel strips. *Mater. Sci. Eng. A* **2021**, *824*, 141796. [\[CrossRef\]](#)
29. Seede, R.; Shoukr, D.; Zhang, B.; Whitt, A.; Gibbons, S.; Flater, P.; Elwany, A.; Arroyave, R.; Karaman, I. An ultra-high strength martensitic steel fabricated using selective laser melting additive manufacturing: Densification, microstructure, and mechanical properties. *Acta Mater.* **2019**, *186*, 199–214. [\[CrossRef\]](#)
30. Rashid, R.R.; Nazari, K.; Barr, C.; Palanisamy, S.; Orchowski, N.; Matthews, N.; Dargusch, M. Effect of laser reheat post-treatment on the microstructural characteristics of laser-cladded ultra-high strength steel. *Surf. Coatings Technol.* **2019**, *372*, 93–102. [\[CrossRef\]](#)
31. Barr, C.; Rashid, R.A.R.; Da Sun, S.; Easton, M.; Palanisamy, S.; Orchowski, N.; Matthews, N.; Walker, K.; Brandt, M. Role of deposition strategy and fill depth on the tensile and fatigue performance of 300 M repaired through laser directed energy deposition. *Int. J. Fatigue* **2020**, *146*, 106135. [\[CrossRef\]](#)
32. Dilip, J.; Ram, G.J.; Starr, T.L.; Stucker, B. Selective laser melting of HY100 steel: Process parameters, microstructure and mechanical properties. *Addit. Manuf.* **2017**, *13*, 49–60. [\[CrossRef\]](#)
33. Seede, R.; Zhang, B.; Whitt, A.; Picak, S.; Gibbons, S.; Flater, P.; Elwany, A.; Arroyave, R.; Karaman, I. Effect of heat treatments on the microstructure and mechanical properties of an ultra-high strength martensitic steel fabricated via laser powder bed fusion additive manufacturing. *Addit. Manuf.* **2021**, *47*, 102255. [\[CrossRef\]](#)
34. Rashid, R.R.; Abaspour, S.; Palanisamy, S.; Matthews, N.; Dargusch, M. Metallurgical and geometrical characterisation of the 316L stainless steel clad deposited on a mild steel substrate. *Surf. Coatings Technol.* **2017**, *327*, 174–184. [\[CrossRef\]](#)
35. Rashid, R.R.; Barr, C.; Palanisamy, S.; Nazari, K.; Orchowski, N.; Matthews, N.; Dargusch, M. Effect of clad orientation on the mechanical properties of laser-clad repaired ultra-high strength 300 M steel. *Surf. Coatings Technol.* **2019**, *380*, 125090. [\[CrossRef\]](#)
36. Vaughan, M.; Samimi, P.; Gibbons, S.; Abrahams, R.; Harris, R.; Barber, R.; Karaman, I. Exploring performance limits of a new martensitic high strength steel by ausforming via equal channel angular pressing. *Scr. Mater.* **2020**, *184*, 63–69. [\[CrossRef\]](#)
37. Shen, C.; Pan, Z.; Ding, D.; Yuan, L.; Nie, N.; Wang, Y.; Luo, D.; Cui, D.; van Duin, S.; Li, H. The influence of post-production heat treatment on the multi-directional properties of nickel-aluminum bronze alloy fabricated using wire-arc additive manufacturing process. *Addit. Manuf.* **2018**, *23*, 411–421. [\[CrossRef\]](#)

38. Chui, P.; Jing, R.; Zhang, F.; Li, J.; Feng, T. Mechanical properties and corrosion behavior of β -type Ti-Zr-Nb-Mo alloys for biomedical application. *J. Alloy. Compd.* **2020**, *842*, 155693. [[CrossRef](#)]
39. Nie, L.; Zhan, Y.; Hu, T.; Chen, X.; Wang, C. β -Type Zr-Nb-Ti biomedical materials with high plasticity and low modulus for hard tissue replacements. *J. Mech. Behav. Biomed. Mater.* **2014**, *29*, 1–6. [[CrossRef](#)]
40. Khalaj, G.; Nazari, A.; Pouraliakbar, H. Prediction of martensite fraction of microalloyed steel by artificial neural networks. *Neural Netw. World* **2013**, *23*, 117–130. [[CrossRef](#)]
41. Bai, Y.; Wang, D.; Yang, Y.; Wang, H. Effect of heat treatment on the microstructure and mechanical properties of maraging steel by selective laser melting. *Mater. Sci. Eng. A* **2019**, *760*, 105–117. [[CrossRef](#)]
42. Liu, F.; Lin, X.; Chen, J.; Song, M.; Han, Y. Fracture mechanism of impact toughness of laser repaired 300M ultra-high strength steel. *Appl. Laser* **2016**, *36*, 635–640. [[CrossRef](#)]